Direct imaging of coexisting ordered and frustrated sublattices in artificial ferromagnetic quasicrystals

B. Farmer,[1] V. S. Bhat,[1] A. Balk,[2,3] E. Teipel,[1] N. Smith,[1] J. Unguris,[2] D. J. Keavney,[4] J. T. Hastings,[5] and L. E. De Long[1,*]
[1] *Department of Physics and Astronomy, University of Kentucky, 505 Rose Street, Lexington, Kentucky 40506-0055, USA*
[2] *Center for Nanoscale Science and Technology, National Institute of Standards and Technology,*
100 Bureau Dr., Gaithersburg, Maryland 20899, USA
[3] *Maryland Nanocenter, University of Maryland, College Park, Maryland 20742, USA*
[4] *Advanced Photon Source 431-E007, Argonne National Laboratory, 9700 S. Cass Ave., Argonne, Illinois 60439, USA*
[5] *Department of Electrical and Computer Engineering, University of Kentucky,*
453F Paul Anderson Tower, Lexington, Kentucky 40506-0046, USA

(Received 30 December 2014; revised manuscript received 9 March 2016; published 25 April 2016)

We have used scanning electron microscopy with polarization analysis and photoemission electron microscopy to image the two-dimensional magnetization of permalloy films patterned into Penrose P2 tilings (P2T). The interplay of exchange interactions in asymmetrically coordinated vertices and short-range dipole interactions among connected film segments stabilize magnetically ordered, spatially distinct sublattices that coexist with frustrated sublattices at room temperature. Numerical simulations that include long-range dipole interactions between sublattices agree with images of as-grown P2T samples and predict a magnetically ordered ground state for a two-dimensional quasicrystal lattice of classical Ising spins.

DOI: 10.1103/PhysRevB.93.134428

I. INTRODUCTION

Bulk quasicrystals exhibit unique physical properties, but are rarely found in nature, and are difficult to grow and characterize in the laboratory [1–3]. Nevertheless, their signature long-range orientational order without periodic translational symmetry places them in a unique niche between periodic crystals and amorphous materials. Specifically, nearest-neighbor atomic coordination in quasicrystals is anisotropic and varies widely [e.g., from 3 to 7 in two-dimensional (2D) Penrose P3 tilings], which is similar to local atomic structures in amorphous solids. On the other hand, quasicrystals are self-similar (any finite area of a tiling is reproduced within a certain distance), and their long-range orientational symmetry (e.g., fivefold-rotational) may be forbidden in periodic crystals [4–6].

A trend of particular interest is that magnetic interactions in known atomic-scale quasicrystals drive only spin glass, rather than long-range magnetic order [1,7,8]. The unique spatial variations in the local energy density and magnitude of moments in magnetic quasicrystals are expected to enhance departures from simple collinear order [5,6,9]. Previous Monte Carlo (MC) simulations of competing exchange and dipole interactions among *microscopic spins* placed on the vertices of 2D decagonal Penrose P3 tilings predict spatial mixtures of "quasiferromagnetic" order and disordered spin glass [5]. In the case of octagonal Ammann-Beenker tilings [6,9], MC simulations including antiferromagnetic exchange interactions and perpendicular anisotropy predict noncollinear "antiferromagnetic" order on interpenetrating sublattices. Nevertheless, the relevance of existing simulations of 2D tilings to the experimental nonexistence of long-range magnetic order in 3D, atomic-scale quasicrystals remains unclear.

Alternatively, advances in nanofabrication permit ferromagnetic thin films to be patterned into ten-nanometer-scale, 2D "artificial quasicrystals" (see Fig. 1). Permalloy films patterned into Penrose P2 tilings (P2T) were recently found to exhibit complex dynamics and nonstochastic magnetic reversal that can be controlled via tiling design, making them a novel class of magnetic metamaterials [4,10]. Herein, we report an initial application of scanning electron microscopy with polarization analysis (SEMPA) to patterned P2T films, which yields direct comparisons of high-resolution images of magnetic textures to numerical simulations of frustration and magnetic order in 2D artificial quasicrystals.

Consideration of a patterned ferromagnetic thin film with two-dimensional P2T topology (see Fig. 1) indicates geometrical frustration will play a strong role in opposing or modifying long-range magnetic order. This situation recalls "artificial spin ices" (ASI), which are thin-film metamaterials that are designed to elucidate the effects of geometrical frustration on magnetic order [11–14]. Most ASI studied to date are disconnected periodic arrays of identical, elongated thin-film segments with symmetric vertices with a single coordination number $N = 3$ or 4. The strong shape anisotropy of ASI segments requires them to behave as macroscopic Ising spins, and leads to a large degeneracy in magnetic dipole energy and a macroscopic (i.e., scaling with system size) contribution to the entropy [11,12]. For example, the honeycomb ASI has a cluster of three symmetrically placed segments surrounding every vertex, and six vertex cluster configurations (out of $2^3 = 8$ possible) that have the same total energy [13,15–17].

However, the frustration found in quasicrystals is very different from that of periodic crystals or amorphous materials, where the dipole energy is uniformly distributed or random in space, respectively. The variations in the asymmetric coordination of vertices in quasicrystals cause variations of the dipole energy and, therefore, the degree of frustration [5]. In the case of connected networks of elongated thin-film segments, we also expect short-range exchange interactions

---

[*] Corresponding author: delong@pa.uky.edu

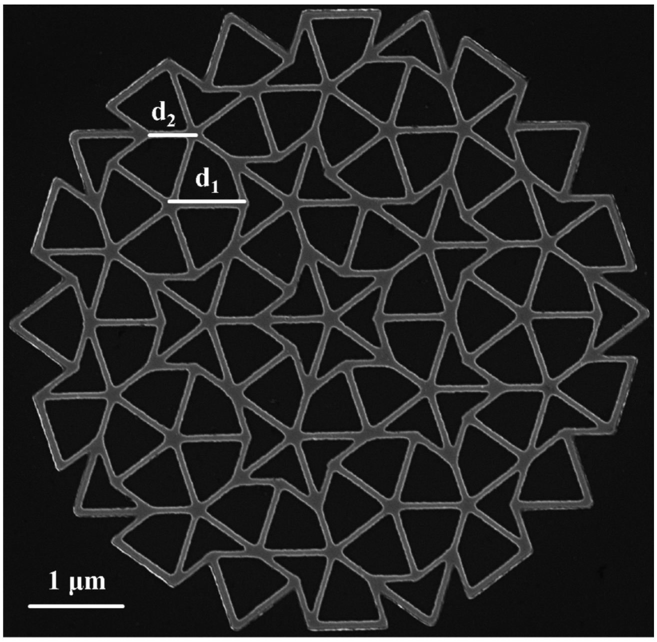

FIG. 1. SEM image of a third generation P2T sample. Bright (dark) regions correspond to permalloy film (Si substrate). Long (d_1) and short (d_2) segment lengths were nominally 810 ± 10 and 500 ± 10 nm, respectively. The width w and thickness t of segments were nominally 70 and 25 nm, respectively. The dumbbell magnetic charge $q = Mwt$ associated with the end of a segment of uniform magnetization M is independent of segment length d. Total apical width of the pattern is 6.8 μm. There are four distinct configurations of $N = 5$ vertices, a single $N = 4$ vertex, two $N = 3$ vertices (one on an edge), and two $N = 2$ edge vertices [see Fig. 4(a)].

in pattern vertices to compete with strong shape anisotropy to stabilize magnetic order; and this is a principal topic of our investigation.

Herein, we report the application of SEMPA [18] to directly image the effects of geometric frustration on magnetic correlations in a connected array of classical Ising spins. Our numerical simulations are in good agreement with room temperature SEMPA images, and predict that third generation P2T will adopt a type of ordered magnetic ground state composed of four magnetic sublattices, one of which has a net magnetic moment. Domain wall (DW) formation within the P2T pattern vertices is found to have a crucial influence on the character of the ordered ground state; and this observation has implications for a wide variety of connected arrays of magnetic thin films.

II. EXPERIMENTAL DETAILS

Sample films were patterned using standard techniques of electron beam lithography. A permalloy ($\mathrm{Ni}_{0.8}\mathrm{Fe}_{0.2}$) film of thickness $t = 25$ nm was deposited at a slow rate of $0.01\ \mathrm{nm} \cdot \mathrm{s}^{-1}$ on a masked Si substrate using electron beam evaporation, followed by a standard lift-off procedure [22].

We generated P2T sample film patterns via the "deflation method" using a graphics algorithm [19–22] incorporated into our electron beam lithography software. Each P2T was patterned as a third generation decahedron truncated to have a 6.8 μm apical width, as shown in the scanning electron microscopy (SEM) image in Fig. 1. Each P2T pattern consists of elongated film segments of two lengths d_1 and d_2 connected at asymmetric vertices having coordination numbers $2 \leqslant N \leqslant 5$. Square arrays of P2T decahedra with 11-μm spacing were fabricated without unpatterned film on substrate borders for photoemission electron microscopy (PEEM) or SEMPA measurements (see Fig. 2).

PEEM images were obtained at room temperature on the as-grown arrays using the Advanced Photon Source beamline 4-ID-C [23]. Samples were mounted in a PEEM instrument with a beam incidence angle of ~16°, providing magnetic sensitivity in the plane of the film along the beam propagation direction. Magnetic maps were taken by tuning the photon energy to the appropriate resonance, in this case the Ni L_3 edge (852 eV),

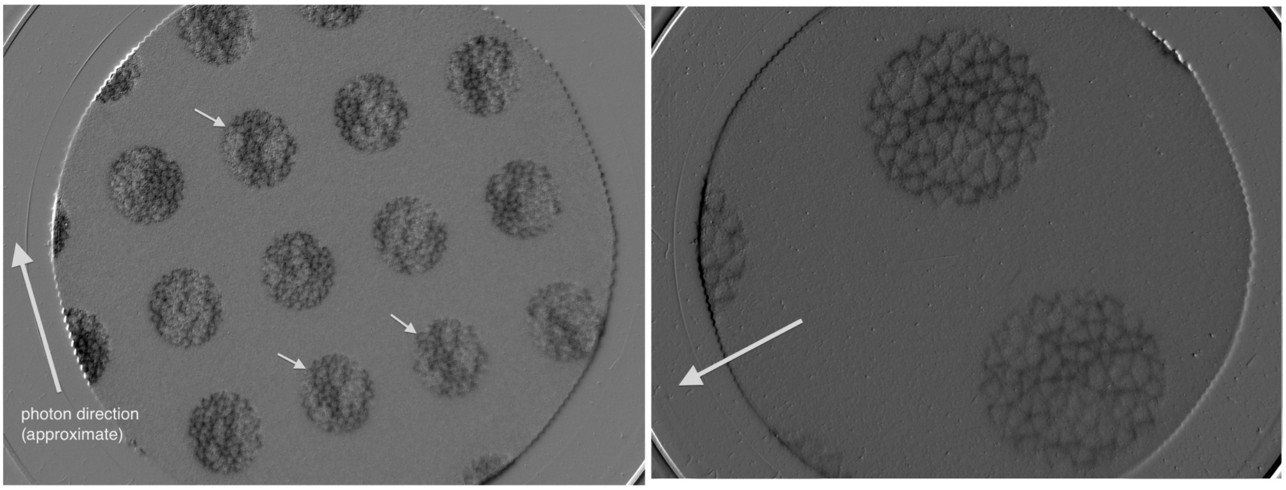

FIG. 2. (Left) PEEM image of a subarea of a 16×16 array of as-grown Penrose P2T patterns, such as shown in Fig. 1 (total apical width of each P2T pattern is 6.8 micrometers). Note that PEEM is only sensitive to magnetization (amplitude represented by gray scale) along the x-ray beam propagation direction (large arrow shown). Three small white arrows indicate P2T having near-identical magnetic textures, which suggests the presence of strong correlations between segment magnetizations. (Right) Close-up PEEM image showing similar textures in two adjacent P2T patterns. Large arrow indicates the x-ray beam direction.

and taking images with right- and left-circularly polarized radiation. The magnetic domain image is then generated by taking the difference of these images, normalized to their sum.

SEMPA operates on the principle that when secondary electrons are ejected from a magnetic sample they maintain their spin polarization, which is detected and correlated with the position of the exciting electron beam to obtain angular and sub-micrometer resolution magnetization maps [24–26]. The spin detector in the SEMPA is set to be simultaneously sensitive to the two in-plane x- and y-magnetization directions, allowing direct measurement of the local magnetization angle without changing the experimental conditions. Moreover, SEMPA is nonperturbative, avoids coupling with fringe fields, and has sufficient angular and submicrometer resolution to characterize DW structures that we find play a critical role in the magnetic properties of P2T [18,26].

After loading the sample into the SEMPA chamber, we clean the sample by exposing it to a 1-keV argon ion beam, which removes <3 nm of material from the surface, including naturally adsorbed oxygen and carbon contaminants. After ion exposure, the cleanliness of the exposed permalloy surface is confirmed by auger spectroscopy. We then deposit 1 to 2 monolayers of iron *in situ*, which is too thin to independently undergo ferromagnetic ordering, but does exchange-couple to the underlying, weaker magnetization of permalloy in order to enhance the domain contrast in the permalloy layer. The thin Fe layer deposited in regions with no permalloy is not ferromagnetic, which was verified by measuring a negligible magnitude for the magnetization in these areas. The Fe layer therefore does not affect the magnetic structure observed within the patterned areas.

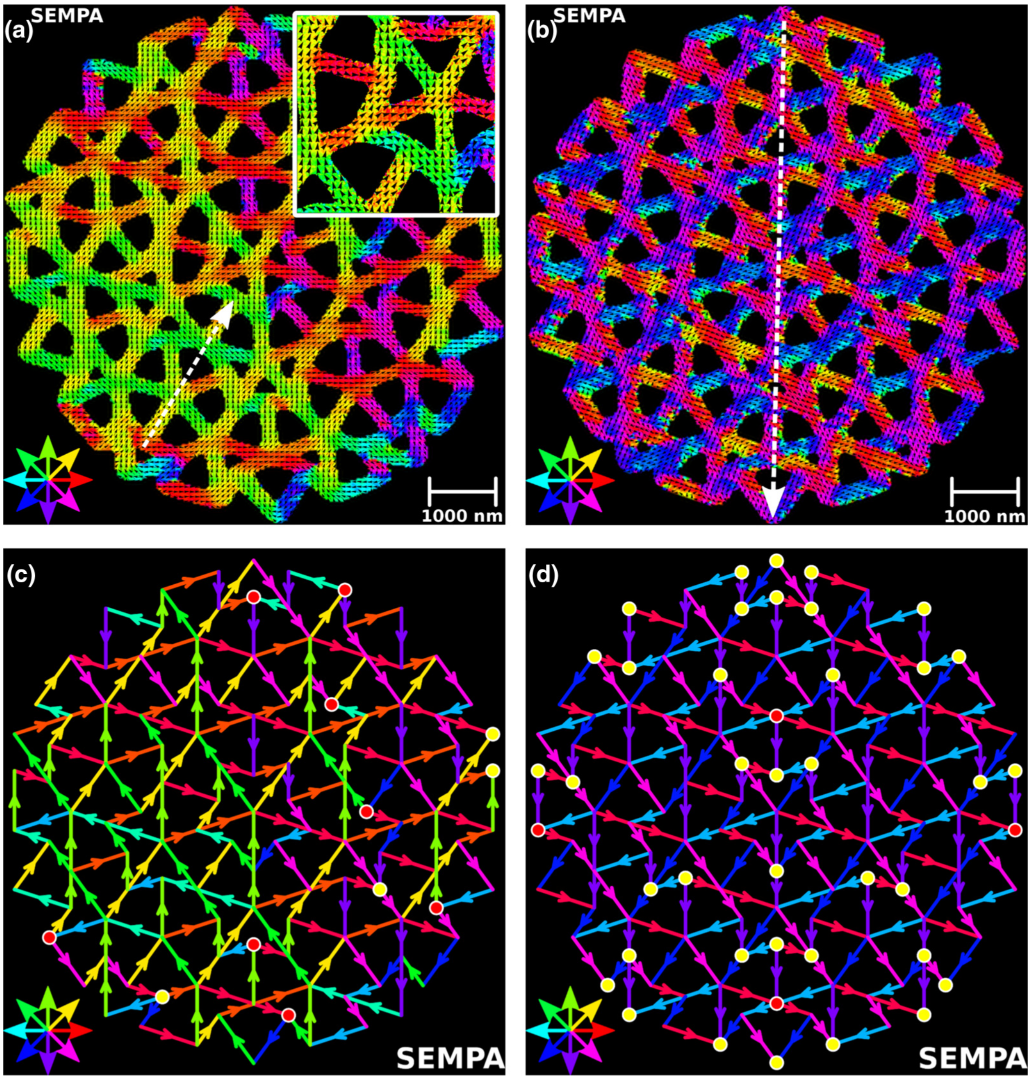

FIG. 3. (a) SEMPA image of as-grown P2T sample 8-2. Color compasses and black arrows denote in-plane magnetization direction. White arrow denotes a flux closure loop extending around central P2T "star". (Inset) High-resolution SEMPA image of DW in the star vertex for low-energy, 2-in/3-out segment configuration. (b) SEMPA image of remnant state after applied field protocol, $H = 0\,\mathrm{A\cdot m^{-1}} \rightarrow +7.96\times10^4\,\mathrm{A\cdot m^{-1}} \rightarrow -7.96\times10^4\,\mathrm{A\cdot m^{-1}} \rightarrow +7.96\times10^4\,\mathrm{A\cdot m^{-1}} \rightarrow 0\,\mathrm{A\cdot m^{-1}}$, along direction of white dotted arrow. (c) Coarse-grained dipole map of (a) showing Ising polarizations defined by colored arrows. Red (yellow) dots indicate high(er)-energy vertices that obey (violate) SIR. (d) Dipole map of (b) exhibiting many violations of SIR (yellow dots). Note perfect mirror symmetry of magnetization about applied field direction in (b) and (d). A complete set of SEMPA images and corresponding dipole maps for all SEMPA samples is given in Ref. [22].

Our micromagnetic simulations show that the DW residing mainly in P2T vertices are of the in-plane Neel type (i.e., no z-component of magnetization), consistent with the 25-nm thickness of the permalloy P2T patterns [27]. SEMPA images of the x- and y-components of the P2T magnetization are transformed into angular maps of the magnetization after removal of a planar background and line-by-line artifacts from each image. The angle of the local magnetization is determined trigonometrically [$\theta = \tan^{-1}(M_y/M_x)$] [see Figs. 3(a) and 3(b)]. The resulting magnetic images are masked with simultaneously obtained secondary electron images to highlight magnetic regions over surrounding nonmagnetic areas [22], which involves choosing a threshold value of the magnetic signal to associate with the P2T structure. Therefore the widths of the segments indicated by the angular map are enlarged due to the electron proximity effect [compare Fig. 1 to Figs. 3(a) and 3(b)]. Nevertheless, the angles θ are accurate with typical measurement uncertainties of less than 10°.

III. PEEM, SEMPA IMAGING RESULTS

An initial survey of a 16×16 P2T array in as-grown condition (i.e., with no prior exposure to applied magnetic fields) was made using PEEM, which is sensitive to a single in-plane component of the film magnetization along the incident x-ray beam propagation direction [23]. Although the aperiodic P2T topology is complex, the PEEM images of as-grown (non-field-cycled) samples reveal striking similarities within small groups of P2T patterns, as shown in Fig. 2. This behavior provides strong evidence that magnetic correlations acting during a slow thin-film deposition have created self-organized, reproducible magnetic textures.

Another 8×8 P2T array was imaged in as-grown condition using SEMPA [see Fig. 3(a)]. Images of the remnant state after field cycling were subsequently acquired [see Fig. 3(b)]. Both as-grown and field-cycled SEMPA images reveal complex textures with segment magnetizations largely aligned along long axes. This is expected, since the high length/width ratio $d_{1,2}/w \geqslant (500\text{ nm}/70\text{ nm}) \approx 7$ of P2T segments favors uniform, binary (i.e., "Ising") segment magnetizations with corresponding magnetic moments $m_{1,2} \propto d_{1,2}$. Coarse-grained averages of P2T segment magnetizations yield simplified maps of mesoscopic Ising spins [see Figs. 3(c) and 3(d)], which suggests that we approximate P2T segment interactions by vertex charge models [28] commonly applied to artificial spin ices (ASI) [29–31].

IV. ANALYSIS OF SEMPA IMAGES

A. Failure of vertex charge models

Interactions between *disconnected* ASI segments are dominated by dipolar interactions that are often treated via simplified vertex charge models ("dumbbell" models–DM) [28,29] in which each Ising spin is replaced by a rigid rod of length l with two equal charges of opposite polarity ($\pm q = \pm(m/l) = \pm(M\times t\times w\times l)/l$) residing at its ends, where m, M, t, and w represent the magnetic dipole moment, the saturation magnetization, the thickness, and the width of a segment, respectively. Note that the magnetic charge q is independent of the dipole length. More generally, vertex charge models simplify the calculation of magnetostatic interaction energies by using a Coulomb interaction between vertex charges that can be written as

$$V(r_{ij}) = \frac{\mu_0}{4\pi}\frac{q_i q_j}{r_{ij}}, \tag{1}$$

where r_{ij} is the distance between the charges q_i and q_j. The magnetic charge density is given by $\rho = -\nabla\cdot\boldsymbol{M}$, which has appreciable value only near the ends of Ising segments. Indeed, most ASI studied to date are *disconnected* ($r_{ij} > 0$ for all $i \neq j$) *periodic arrays of identical, Ising segments*

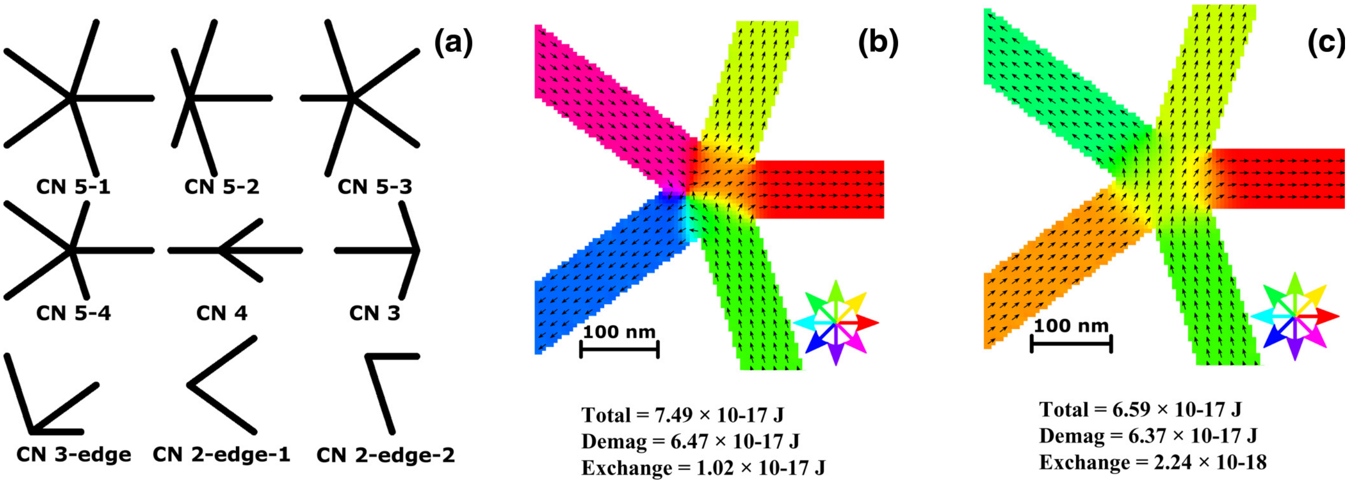

FIG. 4. (a) Nine possible P2T vertex cluster configurations labeled according to asymmetric coordination number CN. The hierarchy of cluster energies for CN5-1 segment polarization arrangements is: 5-in or 5-out, 4-in/1-out or 1-in/4-out, and two energies for 3-in/2-out or 2-in/3-out. (b) Higher-energy, and (c) lower-energy, 2-in/3-out configurations for which OOMMF cluster simulations indicate a 1.6% difference in demag energy, and a 127% difference in exchange energy (listed above). The total cluster energy difference is due to creation of an antivortex (located on the left side of the vertex), resulting in the vertex DW configuration shown in (b), versus a gradually bending texture shown in (c). Note a dumbbell model predicts the opposite order of stability [28] (see Appendix A). The texture in (c) has an overall bottom-to-top polarization having a large CN5-1 cluster net moment that orders via long-range dipole interactions [see Fig. 8(c)]. Note that (c) corresponds well with the SEMPA image in the inset of Fig. 3(a).

with symmetric vertices of a single, low coordination number $N = 3$ or 4 [11,12]. In applications of the DM, the lowest values of vertex energy [defined to be $\sum_{i\neq j} V(r_{ij})$ from Eq. (1)] are attained when the total charge $Q = \sum_i q_i$ near a given vertex is minimal [28]. The latter condition is expressed as a dominant "spin ice rule" (SIR).

The case of P2T is much more complex, given it is an *aperiodic array of Ising segments of two lengths connected at predominantly asymmetric vertices of nine types and a wide range of coordination numbers* $2 \leqslant N \leqslant 5$ [10,19,20] [see Fig. 4(a)]. We therefore adopt an expression derived for the magnetic energy of microscopic spin ices [28]:

$$V(r_{ij}) = \begin{cases} \frac{\mu_0}{4\pi}\frac{q_i q_j}{r_{ij}} & r_{ij} \neq 0 \\ \nu_0 q_i q_j & r_{ij} = 0 \end{cases}. \qquad (2)$$

Although the form of Eq. (2) admits both connected and disconnected arrays of narrow (Ising-like) segments, there is no convention for the location of magnetic charges for a connected ASI in which charges must overlap at a vertex. Nevertheless, if we assume $r_{ij} = 0$ for the nearest-neighbor Ising segments that intersect at a common vertex, Eq. (2) always favors minimal net vertex charge (i.e., for positive ν_o); and we therefore can retain this condition as a SIR upon which we base a modified vertex charge model. The modified SIR can be tested for P2T, as seen in Fig. 5, which is a map of the net vertex charges deduced from the SEMPA image of as-grown sample 8-2 [see Fig. 3(a)]. We note that only 4 out of a total of 121 vertices disobey the modified SIR. However, we will demonstrate that the modified vertex charge model is neither sufficient to explain our SEMPA images, nor can it yield a correct simulated P2T ground state.

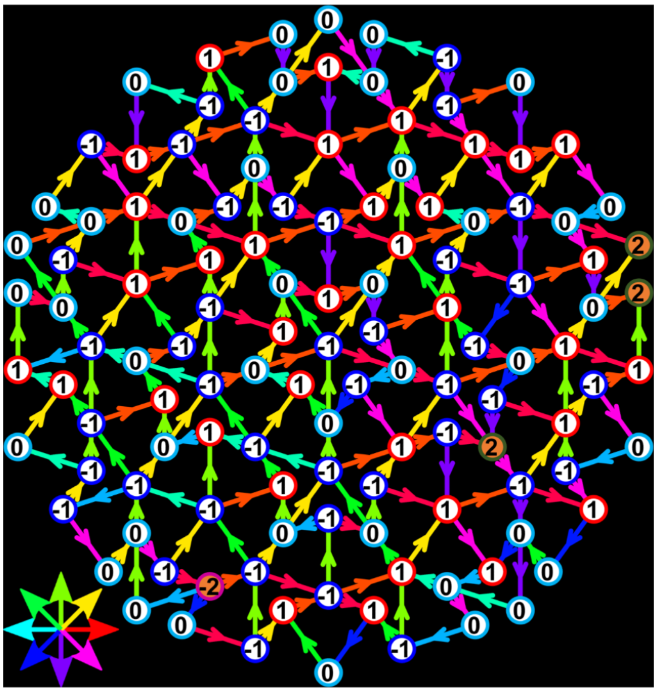

FIG. 5. Dumbbell model analysis of processed SEMPA magnetization map for as-grown P2T sample 8-2 [see SEMPA image in Fig. 3(a)]. Arrows indicate a coarse approximation of the magnetization direction of a corresponding permalloy segment. Arrows are colored according to the color compass at bottom left; their direction also denotes the in-plane magnetization. Numbers indicate net magnetic charge $Q = \sum_i q_i$ at a given vertex; orange-filled (white-unfilled) circles indicate vertices that disobey (obey) the spin ice rule for minimal vertex charge. A complete set of charge maps for all SEMPA samples is given in Ref. [22].

A careful re-examination of the modified vertex charge model to P2T illustrates some *key differences between connected and disconnected wire networks*. As an illustrative example, we address the case of the symmetric, fivefold CN5-1 vertex found in P2T (see Appendix A and Fig. 6). Regardless of the location of charges within a given vertex (e.g., 6–10 in Fig. 6), any asymmetric vertex has two low-energy SIR states that are split due to the unequal distances between the

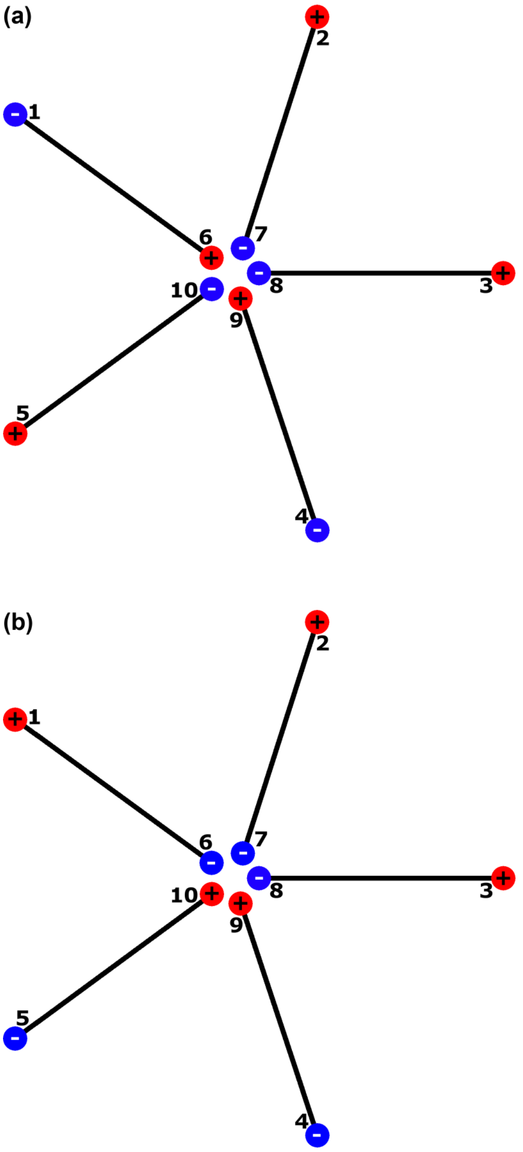

FIG. 6. (a) DM representation of the CN5-1 vertex of Fig. 4(b). Red (blue) indicate positive (negative) charges. If charges labelled 6–10 are considered to be centered on the vertex, we set $r_{ij} = 0$ between them, and apply the rule of Eq. (2). (b) DM representation of the CN5-1 vertex of Fig. 4(c). DM calculations predict configuration (b) to have a higher energy than that of (a), contrasting our OOMMF cluster energy calculations summarized in Fig. 4.

outer charges (e.g., charges 1–5 in Fig. 6). Although some parameters are not fully defined (e.g., ν_o) in Eq. (2), we can still make inferences about the lowest energy states; we have calculated the magnetostatic energies for two SIR states by assuming charges [(1) overlap at the vertex (contributing a self-energy $\propto \nu_0$ due to the assembly of a net charge on a vertex) or (2) do not overlap at the vertex (i.e., there is a well-defined Coulomb interaction between separated charges)]. Regardless of the ambiguous value of ν_o in Eq. (2), both calculations in Appendix A show the magnetostatic energy of the configuration of Fig. 6(b) is higher than that of Fig. 6(a), which is contrary to our SEMPA images and numerical simulations of the magnetostatic energy of P2T discussed below. The above analysis has been applied to all nine vertex types for P2T to demonstrate Eq. (2) cannot produce accurate P2T magnetostatic energies, since it does not model short-range exchange interactions that create and pin DW inside pattern vertices [31].

B. Vertex cluster simulations

The strong shape anisotropy of the P2T segments, combined with the wide variation in the number of nearest-neighbor segments and their asymmetric coordination about a given P2T vertex, lead to a strong variation in the exchange energy density in pattern vertices (an analogous situation has been modelled by defining multiple exchange couplings between near-neighbor spins in atomic quasicrystals [5]). Nevertheless, the vertex DW configurations we observe in anisotropic P2T vertices are repeatable and limited in number; this makes it possible to calculate approximate magnetostatic energies for a finite number of "vertex cluster" configurations of intersecting segments for each of the nine types of vertices present in P2T [see Fig. 4(a)]. These vertex cluster energies can be gathered into a look-up table for use in energy minimization algorithms. The vertex cluster energies thus include an effective "exchange coupling," by supplementing the dipole correlations between P2T segments at the near-neighbor length scale. The vertex cluster simulations show that the exchange energy directly leads to the emergence of ordered P2T sublattices, as discussed in Sec. IV C.

We began a refined energy analysis of P2T magnetic textures by applying the zero-temperature Object Oriented Micro Magnetic Framework (OOMMF) [32] to each of the 2^N possible configurations of nine N-fold "vertex cluster" geometries found in P2T [Fig. 4(a)]. A computer-generated bitmap representation of each cluster type was imported into OOMMF in order to discretize the simulation space into magnetic and non-magnetic regions. OOMMF's internal energy minimizer was then used to obtain the magnetostatic energies of all attainable cluster configurations for the nine vertices in zero applied field.

The permalloy parameters used in OOMMF simulations were as follows: Exchange constant $A = 1.3\times10^{-11}\,\mathrm{J}\cdot\mathrm{m}^{-1}$, saturation magnetization $M_S = 8.6\times10^5\,\mathrm{A}\cdot\mathrm{m}^{-1}$, magnetocrystalline anisotropy constant $K = 0$, gyromagnetic ratio $\gamma = 1.9\times10^9\,\mathrm{Hz}\cdot\mathrm{T}^{-1}$, and dimensionless damping coefficient $\alpha = 0.01$. OOMMF uses the material parameters to calculate a "mean field" $\mathbf{B}_{\mathrm{eff}}$ that is composed of separate demag (E_{dmg}) and exchange (E_{ex}) interaction contributions. The total energy is expressed as $-\boldsymbol{M}\cdot\boldsymbol{B}_{\mathrm{eff}}$, and the exchange energy is assumed to be proportional to $(\nabla M)^2$. Calculations limited to individual vertex clusters therefore favor DW configurations having low magnetization gradients such that $\boldsymbol{M}$ gradually bends through a vertex ["low-energy" in Figs. 4(c) and 3(a), inset], over vertices with DW ["high-energy" in Fig. 4(b)] in which $\boldsymbol{M}$ abruptly twists.

Our SEMPA images of as-grown P2T largely agree with SIR and OOMMF simulations of individual clusters [compare Fig. 4(c) with the CN5-1 texture in Fig. 3(a), inset], but disagree with charge model predictions of vertex cluster polarization [compare Figs. 4(b) to 4(c)]. An exemplary map of Ising dipoles and total vertex charges for as-grown Sample 8-2 is shown in Fig. 5; a corresponding map showing how only a few high-energy vertices violate SIR is given in Fig. 3(c). Additional comparisons of the lowest-energy OOMMF vertex cluster configurations with room-temperature SEMPA images of ten as-grown P2T samples (each with 121 vertices) revealed 104 high-energy vertices (44 of which disobey SIR), which is only 8.6% (3.6%) of the total population (1210) of vertices imaged [22].

Although maps of the net vertex charges (e.g., Fig. 5) for as-grown P2T indicate SIR are nearly always obeyed, the vertex cluster analyses show DW energies are decisive in stabilizing the lowest-energy P2T textures actually observed in our SEMPA images.

C. Monte Carlo simulations of short-range interactions

The small number of high-energy vertices observed in SEMPA images of as-grown P2T suggests they be viewed as dilute topological defects quenched into an ordered ground state. The absence of numerous high-energy defects also suggests relatively weak, longer-range dipolar interactions are necessary to completely stabilize a unique ground state. However, it is impossible to carry out numerical simulations that simultaneously include all possible nearest-neighbor and long-range interactions among P2T segments. Therefore we used an isolated vertex cluster energy to approximate all short-range dipole and exchange interactions obtained from micromagnetic OOMMF simulations. To do this, we considered all of the 2^N possible Ising polarization states for each of the nine P2T vertex cluster types [as indicated in Fig. 4(a)] and calculated the cluster energy for the ith isolated vertex E^i_{cl}, defined as

$$E^i_{\mathrm{cl}} = E^i_{\mathrm{ex}} + E^i_{\mathrm{dmg}}. \qquad (3)$$

Here, E^i_{ex} and E^i_{dmg} are direct outputs from OOMMF. The first exchange energy term reflects the energy cost to create a DW within the given vertex, and the second demagnetization energy term models dipolar interactions between segments.

An approximate "total cluster energy" is then calculated by taking the sum of vertex cluster energies $\sum_i (E^i_{\mathrm{ex}} + \frac{1}{2}E^i_{\mathrm{dmg}})$ for all vertices present in the P2T lattice (with a factor of $\frac{1}{2}$ for the demag contribution to avoid double counting). We then use a simulated annealing MC algorithm to minimize the total cluster energy of the entire P2T [33]. (See Appendix B.) Note that during all MC simulations, all segments are treated as Ising dipoles with binary polarization.

The MC minimization of total cluster energy converged to many different low-energy P2T configurations whose energies

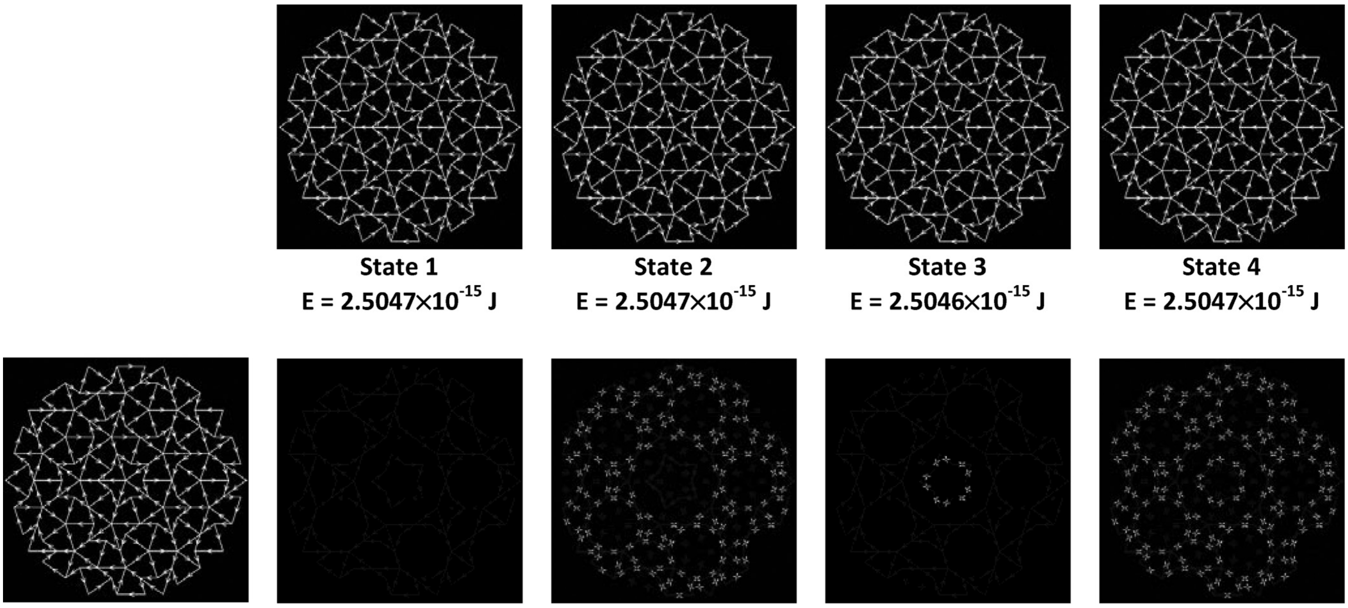

State 1 E = 2.5047×10^{-15} J

State 2 E = 2.5047×10^{-15} J

State 3 E = 2.5046×10^{-15} J

State 4 E = 2.5047×10^{-15} J

State 1 E = 2.5047×10^{-15} J

State 1 – State 1 = null

State 1 – State 2 = SL4

State 1 – State 3 = SL3

State 1 – State 4 = SL3 + SL4

FIG. 7. Matrix comparison of dipole maps for four P2T MC ground states with the State 1 map. Individual MC total cluster energies and the definitions of SL3 and SL4 are shown. Double-arrows indicate segments in opposite polarizations in the two configurations subtracted from one another. An enlarged matrix is given in Ref. [22].

were within 0.0001% of a common value, which is a clear indication of magnetic frustration. Figure 7 shows four of these lowest-energy MC states and their minimized energies. Examination of hundreds of low-energy configurations identified large "sublattices" of connected segments that only appear in a repeated texture, or in the same texture with reversed polarization. Furthermore, there were smaller groups of (e.g., 1 or 2 segments) segments whose switching appeared to be stochastic. Figure 7 illustrates graphical subtractions between four of the low-energy MC states and an arbitrarily chosen "State 1." This subtraction technique identifies two distinct, strongly-correlated (long-range-ordered) sublattices (SL): one is composed of the segments surrounding the P2T "central star" (SL3) and the other is composed of a larger, more complex group of outlying segments (SL4). Segments that do not exhibit large-scale correlated switching were gradually identified, but are darkened in Fig. 7. These segments lie on SL1 or SL2, whose definitions will be clarified below.

The experimental SEMPA image of as-grown sample 8-2 confirms SL3 self-organizes into a clockwise loop on the P2T central star [Fig. 3(a), inset]. A perfectly ordered SL3 star and two SL4 superdomains of larger dipole loops ("swirls") are clearly visible in the corresponding Ising dipole map of the SEMPA image shown in Fig. 8(b). Note all (104) high-energy vertices observed in our P2T samples lie on walls between superdomains in SL4, similar to low-energy textures observed in periodic ASI [34] (see Fig. SI5 in Ref. [22]).

D. Monte Carlo simulations of long-range interactions

Additional simulations were conducted to identify any ordering of SL1 and SL2, by minimizing *only the energy due to long-range dipolar interactions*. We approximated the total P2T magnetostatic energy as a sum of the individual OOMMF vertex cluster energies (that include short-range dipole and exchange interactions), supplemented by longer-range dipole interactions needed to order SL1 and SL2. The MC simulation replaced segment magnetizations with point Ising dipoles located in the centers of segments; but SL1 and SL2 dipoles were the only ones allowed to fluctuate, while the ordered dipoles in SL3 and SL4 were held fixed. Furthermore, all dipole variations on SL1 and SL2 were constrained to restrict vertex cluster configurations to their lowest-energy states. The resulting small variations in dipolar energy were calculated with the standard expression:

$$E = \sum_{j>k} \frac{\mu_0}{4\pi r_{jk}^3}[3(\boldsymbol{m}_j \cdot \hat{\mathbf{e}}_{jk})(\boldsymbol{m}_k \cdot \hat{\mathbf{e}}_{jk}) - \boldsymbol{m}_j \cdot \boldsymbol{m}_k]. \quad (4)$$

The long-range dipolar interaction energy was minimized according to a simulated annealing protocol that began at a sufficiently high temperature that any of the SL1 and SL2 segment configurations were equally probable (i.e., above the ordering temperatures of SL1 and SL2). Note that this procedure accurately reflects the persistent experimental observations in room temperature SEMPA images of order on highly-correlated SL3 and SL4, as well as the lack of order observed in SL1 and SL2.

As expected, different MC runs yielded a number of degenerate P2T textures in which various initial choices for two ordered sublattices, SL3 and SL4, were held fixed [see Figs. 8(a) and 7]. Closer inspection revealed the MC converged to ten equivalent dipolar orderings that reflected the fivefold rotational and spin inversion symmetries of the order parameter of a single ground state phase shown in Fig. 8(a). Segments not in SL3 or SL4 were assigned to two additional sublattices, according to their symmetries in the fully ordered state [see Fig. 8(a)]: SL2 (magenta) segments were radially aligned with

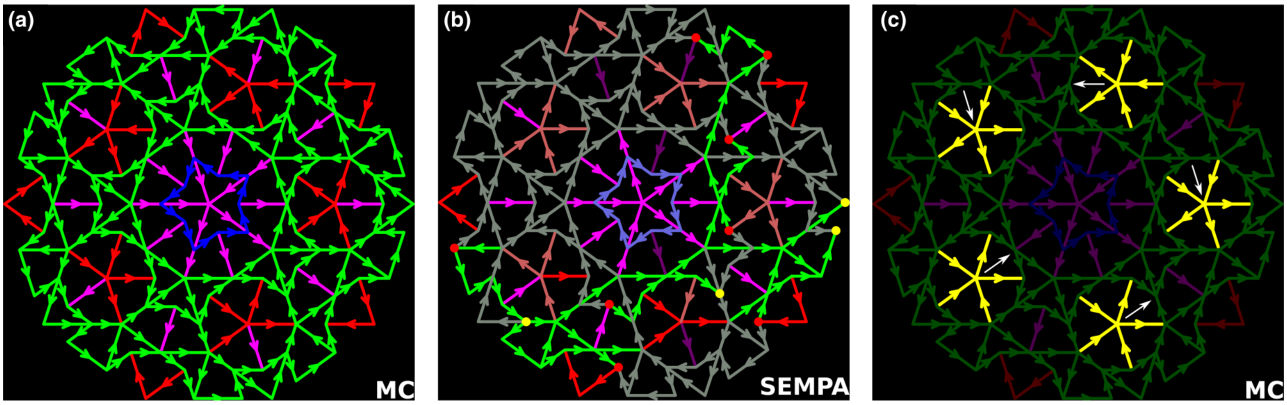

FIG. 8. (a) Dipole map of ordered MC ground state induced by long-range dipole interactions. SL1 (red) dipoles swirl with 5-fold rotational symmetry and no net moment. SL2 (magenta) dipoles exhibit mirror symmetry about a net ferromagnetic axis. SL3 (dark-blue) and SL4 (green) dipole swirls are correlated by cluster interactions. (b) Sublattice map for SEMPA image of as-grown sample 8-2 [shown in Figs. 2(a) and 2(c)]. An ordered SL3 is colored light blue. Two ordered SL4 superdomains are colored grey (clockwise vorticity) and lime-green (counter-clockwise vorticity), respectively. Salmon dipoles are disordered SL1 segments, and magenta dipoles are disordered SL2 segments. Superdomains are separated by red (yellow) dots that are high(er)-energy vertices obeying (disobeying) SIR. Low-energy vertices obeying SIR are not highlighted. A complete set of dipole maps for all our SEMPA images is given in Ref. [22]. (c) MC ground state of (a) altered by substitution of one of 10 configurations of the CN5-1 segments (highlighted in yellow) with degenerate total cluster energies. SL1 and SL2 segment polarizations in CN5-1 are not affected by SL4 order in cluster-energy MC, as shown by white arrows that denote (disordered) net CN5-1 cluster moments.

mirror symmetry about a net magnetic moment direction, and SL1 (red) segments ordered into another swirled texture with no net moment and fivefold rotational symmetry about the center of the P2T pattern.

E. Frustration and degeneracy in P2T

The cluster MC analysis makes it clear that the peculiar aperiodic P2T topology with one symmetrically- and eight asymmetrically-coordinated vertices induces reproducible, low-energy vertex DW textures that reflect strong, nearest-neighbor correlations that completely order SL3 and SL4 above room temperature. We have found that every room-temperature SEMPA image of as-grown P2T can be deconstructed into spatially distinct, coexisting sublattices: two are frustrated (SL1, SL2) and two are ordered (SL3, SL4), as shown in Fig. 8(b).

Segments in SL1 and SL2 remain disordered at room temperature because one or both of the odd-N vertices to which they connect remain in a low-energy state regardless of the polarization of the connecting segment. For example, the CN5-1 vertex clusters self-organize into slow-bending vertex textures (i.e., with small $|\nabla M|$) with the same low vertex cluster energy, resulting in large net cluster moments that remain free to rotate (and are therefore frustrated) with respect to surrounding SL4 vertices [see Fig. 8(c)]. Each one of the five CN5-1 clusters can therefore adopt five nearly-degenerate angular orientations, each with two possible time-reverse polarizations. The degeneracy contributed by the five CN5-1 vertices is therefore $\{(5\,\text{textures})\times(2\,\text{polarizations})\}^5 = 10^5$. Note that the exponent 5 (i.e., the number of CN5-1 vertices with SL1 segments) scales with the size of the P2T sample; the corresponding entropy contribution, which is proportional to the logarithm of the degeneracy, therefore scales linearly with the sample size, making it "macroscopic."

Inclusion of additional disordered vertices [which occupy SL1 and SL2 defined in Fig. 8(a)] yields a total number of 3.28×10^{10} macrostates that share the minimum MC total cluster energy, and generates a large macroscopic entropy contribution required of an ASI [11,12]. The calculation of P2T degeneracy is discussed in more detail in Appendix C.

V. DISCUSSION

A. Long-range magnetic order in P2T

The previous section shows that the residual frustration and degeneracy in SL1 and SL2, which express the ASI character of P2T at room temperature, are unusual, in that they are *dictated by the emergent magnetic order on SL3 and SL4*: Fig. 8(b) gives an example of a highly frustrated and partially ordered state at room temperature. A qualitatively similar, partially ordered state was found in MC simulations of *atomic spins* placed on a 2D Penrose P3 tiling [5], but was never verified by experiment. The mesoscopic, swirling textures of the MC ground state shown in Fig. 8(a) are very different from those proposed for periodic, honeycomb [15,30], and square [15,35] ASI, where dipole interactions favor nanoscale closed loops ("vortices") of near-neighbor segments [15,29,30,35–37]. The P2T ground state also differs from the disordered, frustrated textures recently reported for the periodic disconnected Shakti lattice that also has mixed vertex coordination ($N = 2,3,4$) [37].

B. Energy barriers to P2T equilibration

We observe field-cycled P2T behave in a manner distinctly different from as-grown samples. SEMPA images acquired in the field-cycled remnant state [Figs. 3(b) and 3(d)] exhibit many high-energy vertices and near-perfect mirror symmetry with respect to the magnetic field axis, which confirms the high quality of our P2T samples and verifies the existence of a "near-saturated" Ising remnant state anticipated from dc magnetization and ferromagnetic resonance studies of third generation P2T [10].

We have observed that the Ising remnant state persists in SEMPA samples for at least 10 to 100 hours after modest field cycling between $H = 0\,\mathrm{A \cdot m^{-1}}$ and $\pm 7.96 \times 10^4\,\mathrm{A \cdot m^{-1}}$. This is consistent with the presence of energy barriers $\approx 10^5$ K, which suppress full equilibration of magnetization in micrometer-scale ASI film segments of comparable dimensions at room temperature [11,12], as well as the fact that the ferromagnetic phase transition of a 25-nm-thick permalloy film is placed well above room temperature [38]. The coexistence of superdomains of swirled order in SL3 and SL4 with disorder on frustrated SL1 and SL2, is also consistent with the presence of large energy barriers to equilibration.

We emphasize that our field cycling protocol (see Fig. 3) is not intended to enhance equilibration of the P2T ground state: Although demagnetization protocols based on field variations are known to improve obedience of ASI to SIR, they are not effective at promoting a magnetic ground state [11,14,17,39]. We believe the striking differences we observe between as-grown and field-cycled remnant states (see Figs. SI5 and SI6 and Table SI1 [22]) indicate the low permalloy deposition rate ($0.01\,\mathrm{nm \cdot s^{-1}}$) we used permits samples to access a significant number of microstates before the segment blocking temperature is reached during film deposition [40–42].

Our MC simulations and SEMPA images imply third generation P2T undergo one or more phase transitions that result in swirled magnetic order on SL3 and SL4 above room temperature. Our MC simulations of longer-range dipole interactions suggest additional phase transitions will yield swirled order on SL1, and radially directed order with a net magnetic moment on SL2 [see Fig. 8(a)]. However, any future search for magnetic phase transitions on P2T sublattices must include a protocol that is effective at lowering barriers to full equilibration of P2T samples. Several methods may prove useful, including thinning film segments to enhance fluctuations [43], annealing samples near their Curie temperature [34,37], and/or depositing film materials with Curie temperatures nearer room temperature [44–46].

C. P2T as an artificial spin ice

We find connected, aperiodic P2T exhibit several similarities to periodic ASI (e.g., square or honeycomb) arrays [11,12]:

(1) The strong shape anisotropy of thin-film segments stabilize near-uniform, bipolar magnetizations that approximate Ising spins that largely obey SIR in low applied magnetic fields, as anticipated in Ref. [10].

(2) Magnetostatic simulations of short-range interactions among nearest-neighbor P2T segments sharing a common pattern vertex yield a large degeneracy among the low-energy magnetization textures, due to geometrical frustration.

(3) SEMPA images of as-grown P2T samples exhibit striking differences from those of field-cycled samples, which strongly suggests large energy barriers prevent full equilibration to an ordered ground state, as observed in periodic ASI with comparable film thickness.

On the other hand, the connected, asymmetric P2T vertices introduce behaviors distinctly different from those of periodic ASI studied to date.

(4) Reproducible vertex DW split the low-energy degeneracies differently than predicted by vertex charge models that are commonly applied to disconnected, periodic ASI.

(5) We have inferred mesoscopic “swirled” magnetic order with no net moment for three P2T sublattices, which contrasts with the much smaller magnetization loops of unit-cell-dimension observed in ground-state textures of periodic ASI [15,29,30,35–37].

VI. SUMMARY AND CONCLUSION

(1) We have acquired direct two-dimensional SEMPA images of frustrated magnetization textures in patterned ferromagnetic thin films.

(2) Reproducible DW textures are observed within various types of asymmetrically coordinated vertices required by the five-fold rotational symmetry and aperiodicity of P2T.

(3) Vertex DW regulate nearest-neighbor exchange and dipole interactions that induce an unusual swirled order within two spatially distinct P2T sublattices that coexist with two frustrated sublattices at room temperature.

(4) Monte Carlo simulations predict long-range dipole interactions will establish magnetic order in the two frustrated sublattices, yielding a net moment at low temperatures, which differs from ground states of known periodic ASI.

(5) The ordered ground state simulated for an artificial P2T of classical Ising spins sharply contrasts with the persistent nonobservation of long-range magnetic order in bulk quasicrystals [5–8]. The agreement between our MC simulations and our SEMPA images strongly suggest a fully ordered magnetic ground state will be confirmed in future studies of better-equilibrated P2T.

Finally, our results show that the variety of vertex coordinations and symmetries exhibited by known quasicrystalline tilings [1–3,19,20] and Shakti lattices [37] will provide a rich set of metamaterials for highly controlled experimental and numerical studies of effects of frustration and aperiodicity on magnetic order and spin ice behavior. In particular, the significance of our results with respect to previous MC simulations [5,6] of mi*croscopic* spins located on vertices of 2D Penrose P3 and Ammann-Beenker tilings remains to be resolved.

ACKNOWLEDGMENTS

Research at University of Kentucky was supported by U.S. DoE Grant DE-FG02-97ER45653, U.S. NSF Grant DMR-1506979, the UK Center for Advanced Materials, the UK Center for Computational Sciences, and the UK Center for Nanoscale Science and Engineering. AB acknowledges support of this research under the Cooperative Research Agreement between the University of Maryland and National Institute of Standards and Technology Center for Nanoscale Science and Technology, Award 70NANB10H193, through the University of Maryland. Research at the Advanced Photon Source, a U.S. Department of Energy Office of Science User Facility operated by Argonne National Laboratory, was supported under Contract No. DE-AC02-06CH11357. J. P. Straley, K. Ross, and F. Guo contributed helpful criticism.

APPENDIX A

Here we describe two ways to calculate the DM energies for the SIR states indicated in Fig. 6 by assuming charges either overlap at the vertex (contributing a self-energy due to assembly of charges on a vertex), or they do not (resulting in a Coulomb interaction between separated charges on a vertex). First, we apply Eq. (2) for the case when the vertex charges overlap:

1. 2-in / 3-out [Fig. 6(a) configuration]

$$E_a = \sum_{i\neq j} V(r_{i,j}), \tag{A1}$$

$$E_a = V(r_{1,2}) + V(r_{1,3}) + \cdots + V(r_{9,10}), \tag{A2}$$

$$E_a = -2\nu_0 q^2 - \frac{\mu_0 q^2}{4\pi}\left(\frac{1}{r_{1,6}} + \frac{3}{r_{1,2}} - \frac{1}{r_{1,3}}\right). \tag{A3}$$

2. 2-in / 3-out [Fig. 6(b) configuration]

$$E_b = \sum_{i\neq j} V(r_{i,j}), \tag{A4}$$

$$E_b = V(r_{1,2}) + V(r_{1,3}) + \cdots + V(r_{9,10}), \tag{A5}$$

$$E_b = -2\nu_0 q^2 - \frac{\mu_0 q^2}{4\pi}\left(\frac{1}{r_{1,6}} - \frac{1}{r_{1,2}} + \frac{3}{r_{1,3}}\right). \tag{A6}$$

The DM calculation for overlapping charges shows the configuration corresponding to Fig. 6(b) has higher energy than that of Fig. 6(a), since the net energy difference calculated using Eq. (2) is positive:

$$\Delta E = E_b - E_a = \frac{\mu_0 q^2}{\pi r_{1,2} r_{1,3}}(r_{1,3} - r_{1,2}). \tag{A7}$$

Note the undefined terms proportional to ν_o cancel out in the energy difference ΔE, since $r_{1,2} = r_{2,3} = \cdots = r_{5,1}$ (nearest neighbor distances are equal), $r_{1,6} = r_{2,7} = \cdots = r_{5,10}$ (segment lengths are equal), and $r_{1,3} = r_{2,4} = \cdots = r_{5,2}$ (second nearest neighbor distances are equal).

In cases where charges have finite separation at the vertex, the ν_o terms do not exist (since we now assume $r_{ij} \neq 0$), and the energy difference calculations yield:

$$\Delta E = \frac{\mu_0 q^2}{\pi}\left[\frac{r_{1,3} - r_{1,2}}{r_{1,2} r_{1,3}} + 5\left(\frac{r_{6,8} - r_{6,7}}{r_{6,7} r_{6,8}}\right)\right]. \tag{A8}$$

Since $r_{6,7} = r_{7,8} = \cdots = r_{9,10}$ (nearest neighbors within a vertex are equidistant) and $r_{6,8} = r_{7,10} = \cdots = r_{10,7}$ (second nearest neighbors within a vertex are equidistant), the second calculation again indicates the energy of the configuration of Fig. 6(b) is larger than that of Fig. 6(a), as indicated by a positive ΔE. *This energy hierarchy is contrary to our OOMMF vertex cluster calculations* described in Fig. 4.

APPENDIX B

We used the simulated annealing procedure to minimize the total cluster energy of the entire P2T, which includes only short-range interactions. A second application of the algorithm minimized the long-range dipolar interactions. For minimizing short-range interactions (total cluster energy), the P2T is initialized with a random configuration of Ising segment polarizations throughout the P2T. The application for long-range interactions began with a random configuration of Ising segments on SL1 and SL2 while SL3 and SL4 were held in one of their ordered configurations.

The minimization algorithm begins with proposing a random, single-segment flip. The change in total cluster energy due to the segment flip is calculated and, if the energy difference is less than zero, the flip is accepted; if not, the energy difference is compared to a thermal bath energy by means of a Boltzmann factor whose arguments are the bath temperature and the input energy difference. A random number is then generated; if the Boltzmann factor is greater than the random number, the flip is accepted. The temperature of the thermal bath is initially set such that most proposed segment flips are accepted. The temperature is then allowed to decrease as the simulation progresses. The simulation stops when there are multiple decreases in temperature with no further decrease in summed cluster energy.

APPENDIX C

We now provide details of the calculation of degeneracies of the various clusters defined in Fig. 4(a). We choose CN5-1 as an exemplary cluster that is embedded within an ordered SL4, and illustrated in Fig. 8(c). Five segments combine to make each CN5-1 vertex; of the five segments, three connect to a CN3 vertex and two connect to a CN5-4 vertex. All five segments can be in one of two Ising states, therefore there are $2^5 = 32$ separate configurations available to the CN5-1 cluster. The CN5-4 and CN3 vertices are partially ordered due to SL4 ordering and have only one free segment (the one shared with the CN5-1 vertex). Therefore SL4 ordering does not impose any constraints on the segment orientations of the embedded CN5-1 vertex, which also must maintain minimum cluster energy: the state of each CN5-1 vertex must be such that segment polarizations are either 2-in/3-out or 3-in/2-out, *and the magnetization must flow through the vertex to avoid strong magnetization gradients in domain walls*. There are ten states out of the 32 which obey these conditions. This contributes a degeneracy factor of 10^5, as there are five of these vertices embedded in the P2T. Note each CN5-1 vertex has a net magnetic moment that interacts with the surroundings on a long-range dipole energy scale lower than the cluster energy resolves. This remains true throughout the following discussion of all SL1 and SL2 vertices.

The central CN5-1 vertex also has five segments, each of which is connected to a CN4 vertex. These CN4 vertices have tangential segments that are *already ordered* via nearest-neighbor interactions on SL3. Therefore, for the CN4 vertices to be in low-cluster-energy states, the radially directed segments must be such that one is pointing in and one is pointing out. Since there are five segments shared between the central CN5-1 vertex and the CN4 vertices, there are only ten low-energy configurations available. This brings our total degeneracy factor up to $10^5 \times 10 = 1 \times 10^6$.

The remaining CN2-edge-2 vertices (part of SL1) connect to CN3 vertices of SL4. The strong nearest-neighbor correlations of SL4 force CN3 vertices to be in low-cluster-energy states, regardless of the polarization of the shared segment with the CN2-edge-2 vertex. Therefore the only constraint is 1-in/1-out for the CN2-edge-2 vertex, meaning there is a degeneracy of 2^5 due to these vertices. This yields $10^5 \times 10 \times 2^5$ for our total degeneracy factor.

Finally, the remaining segments of SL2 are separated from one another, and shared between a CN5-2 vertex and a CN3 vertex. Both CN5-2 and CN3 vertices, partially ordered by SL4, are in low-cluster-energy states, regardless of the polarization of the single SL2 segment. This means there is a 2-fold degeneracy for each of the ten SL2 segments, adding a degeneracy factor of 2^{10}, for a total degeneracy of $10^5 \times 10 \times 2^5 \times 2^{10}$, which yields a net degeneracy of 3.2768×10^{10}.

Thus we see the degeneracy contributed by unresolved segments in SL1 and SL2 is driven by the nearest neighbor interactions that induce order on SL3 and SL4. Therefore Figs. 8(b) and 8(c) are examples of highly frustrated (and partially ordered) P2T states.

[1] J.-M. Dubois, *Useful Quasicrystals* (World Scientific, Singapore, 2005).
[2] P. Thiel, Nat. Mater. **6**, 11 (2007).
[3] M. de Boissieu, Nat. Mater. **12**, 692 (2013).
[4] V. S. Bhat, B. Farmer, N. Smith, E. Teipel, J. Woods, J. Sklenar, J. B. Ketterson, J. T. Hastings, and L. E. De Long, Physica C **503**, 170 (2014).
[5] E. Y. Vedmedenko, H. P. Oepen and J. Kirschner, Phys. Rev. Lett. **90**, 137203 (2003).
[6] E. Y. Vedmedenko, U. Grimm, and R. Wiesendanger, Phys. Rev. Lett. **93**, 076407 (2004).
[7] A. I. Goldman, Sci. Technol. Adv. Mater. **15**, 044801 (2014).
[8] G. Gebresenbut, M. Andersson, P. Beran, P. Manuel, P. Nordblad, M. Sahlberg, and C. Gomez, J. Phys.: Condens. Matter. **26**, 322202 (2014).
[9] S. Wessel, A. Jagannathan, and S. Haas, Phys. Rev. Lett. **90**, 177205 (2003).
[10] V. S. Bhat, J. Sklenar, B. Farmer, J. Woods, J. T. Hastings, S. J. Lee, J. B. Ketterson, and L. E. De Long, Phys. Rev. Lett. **111**, 077201 (2013).
[11] C. Nisoli, R. Moessner, and P. Schiffer, Rev. Mod. Phys. **85**, 1473 (2013).
[12] L. J. Heyderman and R. L. Stamps, J. Phys.: Condens. Matter. **25**, 363201 (2013).
[13] M. Tanaka, E. Saitoh, H. Miyajima, T. Yamaoka, and Y. Iye, J. Appl. Phys. **97**, 10J710 (2005).
[14] R. F. Wang, C. Nisoli, R. S. Freitas, J. Li, W. McConville, B. J. Cooley, M. S. Lund, N. Samarth, C. Leighton, V. H. Crespi, and P. Schiffer, Nature (London) **439**, 303 (2006).
[15] G. Möller and R. Moessner, Phys. Rev. Lett. **96**, 237202 (2006).
[16] Y. Qi, T. Brintlinger, and J. Cumings, Phys. Rev. B **77**, 094418 (2008).
[17] E. Mengotti, L. J. Heyderman, A. Fraile Rodríguez, Á. Bisig, L. Le Guyader, F. Nolting, and H. B. Braun, Phys. Rev. B **78**, 144402 (2008).
[18] M. Scheinfein, J. Unguris, M. Kelley, D. Pierce, and R. Celotta, Rev. Sci. Instrum. **61**, 2501 (1990).
[19] B. Grünbaum and G. C. Shephard, *Tilings and Patterns* (W. H. Freeman & Co., New York, 1987).
[20] R. Penrose, Math. Intell. **2**, 32 (1979).
[21] A. Glassner, IEEE Comp. Graph. Appl. **18**, 83 (1998).
[22] See Supplemental Material at http://link.aps.org/supplemental/10.1103/PhysRevB.93.134428 for additional information regarding sample film fabrication, SEMPA imaging procedures, P2T sublattice identification procedures, and a complete set of all SEMPA images obtained in this study.
[23] X. M. Cheng and D. J. Keavney, Rep. Prog. Phys. **75**, 026501 (2012).
[24] S. R. Bowden and J. Unguris, J. Appl. Phys. **114**, 223904 (2013).
[25] R. Frömter, H. Stillrich, C. Menk, and H. P. Oepen, Phys. Rev. Lett. **100**, 207202 (2008).
[26] S.-H. Chung, R. D. McMichael, D. T. Pierce, and J. Unguris, Phys. Rev. B **81**, 024410 (2010).
[27] S. Middelhoek, J. Appl. Phys. **34**, 1054 (1963).
[28] C. Castelnovo, R. Moessner, and S. L. Sondhi, Nature (London) **451**, 42 (2008).
[29] G. Möller and R. Moessner, Phys. Rev. B **80**, 140409(R) (2009).
[30] G.-W. Chern, P. Mellado, and O. Tchernyshyov, Phys. Rev. Lett. **106**, 207202 (2011).
[31] Y. C. Shen, O. Petrova, P. Mellado, S. Daunheimer, J. Cumings, and O. Tchernyshyov, New J. Phys. **14**, 035022 (2012).
[32] M. J. Donahue and D. G. Porter, *OOMMF User's Guide, Version 1.0*. Interagency Report NISTIR 6376 (National Institute of Standards and Technology, Gaithersburg, MD, 1999).
[33] S. Kirkpatrick, J. Stat. Phys. **34**, 975 (1984).
[34] S. Zhang, I. Gilbert, C. Nisoli, M. J. Erickson, L. O'Brien, C. Leighton, P. E. Lammert, V. H. Crespi, and P. Schiffer, Nature (London) **500**, 553 (2013).
[35] L. A. S. Mol, W. A. Moura-Melo, and A. R. Pereira, Phys. Rev. B **82**, 054434 (2010).
[36] W. R. Branford, S. Ladak, D. E. Read, K. Zeissler, and L. F. Cohen, Science **335**, 1597 (2012).
[37] I. Gilbert, G.-W. Chern, S. Zhang, L. O'Brien, B. Fore, C. Nisoli, and P. Schiffer, Nat. Phys. **10**, 670 (2014).
[38] D. Mauri, D. Scholl, H. C. Siegmann, and E. Kay, Appl. Phys. A **49**, 439 (1989).
[39] Z. Budrikis, J. P. Morgan, J. Akerman, A. Stein, P. Politi, S. Langridge, C. H. Marrows, and R. L. Stamps, Phys. Rev. Lett. **109**, 037203 (2012).
[40] J. P. Morgan, A. Stein, S. Langridge, and C. H. Marrows, Nat. Phys. **7**, 75 (2011).
[41] C. Nisoli, New J. Phys. **14**, 035017 (2012).
[42] S. J. Greaves and H. Muraoka, J. Appl. Phys. **113**, 17B517 (2013).
[43] A. Farhan, A. Kleibert, P. M. Derlet, L. Anghinolfi, A. Balan, R. V. Chopdekar, M. Wyss, S. Gliga, F. Nolting, and L. J. Heyderman, Phys. Rev. B **89**, 214405 (2014).
[44] U. B. Arnalds *et al.*, Appl. Phys. Lett. **101**, 112404 (2012).
[45] V. Kapalakis *et al.*, New J. Phys. **14**, 035009 (2012).
[46] J. Drisko, S. Daunheimer, and J. Cumings, Phys. Rev. B **91**, 224406 (2015).